Pressure and saturation changes estimated from extended elastic impedance properties using time-lapse seismic data: Enfield Field, NW Australia

Sergey Shevchenko[1] and Wayne D. Pennington[2]

https://doi.org/10.1190/tle41110777.1

Abstract

The extended elastic impedance (EEI) concept has been used in the oil industry primarily for lithology and fluid prediction in exploration and development projects. We present a method of reservoir monitoring that identifies and maps changes in pressure and saturation in a producing reservoir by applying EEI to time-lapse seismic data. The method uses time-lapse seismic difference data rotated to specific EEI χ angles that are optimized for the changes expected in a given reservoir. One angle is found to be appropriate to identify predicted changes in saturation, using fluid-substitution models, while the other angle is found from rock-physics assumptions or laboratory measurements of fluid-pressure changes. Our technique is tested using time-lapse seismic data from the Enfield oil field in Australia's North West Shelf, with estimates of optimal EEI rotation angles χ based on log data and Biot-Gassmann modeling for the fluid changes ($\chi = +42^\circ$) and on rock-physics models fit to measurements made on core samples for the pressure changes ($\chi = -79^\circ$). Seismic reflectivity and inversion domains were used for comparison and analysis of the final rotated volumes. We used publicly available seismic data that had been recorded and processed in 2004 and 2007 when time-lapse processing was still being developed. The low reproducibility of these seismic data and the complexity of the reservoir architecture limited the extent of our interpretation and results. Nonetheless, our qualitative and quantitative results are encouraging and supported by field production data. This technically simple approach should be useful in the analysis of time-lapse seismic data processed by modern techniques and would help in the management of reservoirs using a straightforward and readily reproduced procedure.

Methodology background

The extended elastic impedance (EEI) methodology was introduced by Whitcombe (2002) and is used mainly for lithology and fluid prediction using amplitude variation with offset (AVO) properties of the seismic data. Prior to that, the elastic impedance (EI) concept covered the observable range of incident angles (Connolly, 1999; Hendrickson, 1999), based on the simplified two-parameter version of Shuey's (1985) approximation to the reflection coefficient R:

$$R(\theta) = A + B \sin^2 \theta, \tag{1}$$

where A is intercept and B is gradient with θ the angle of the incidence. With this two-parameter model, two elastic properties may be estimated from the AVO trends; usually these are the P-wave velocity (V_P) and the S-wave velocity (V_S) (or the V_P/V_S ratio).

Connolly (1999) introduced EI as a generalization of acoustic impedance (AI) for variable incidence angle and defined it as

$$EI(\theta) = V_P^a V_S^b \rho^c, \tag{2}$$

where $a = 1 + \sin^2 \theta$, $b = -8k \sin^2 \theta$, $c = (1 - 4k \sin^2 \theta)$, and $k = [V_S/V_P]^2$.

Whitcombe (2002) found a normalized version of EI by using average values of V_P, V_S, and ρ and defined normalized EI as

$$EI(\theta) = V_{P0}\, \rho_0\, [(V_P/V_{P0})^a\, (V_S/V_{S0})^b\, (\rho_p/\rho_0)^c], \tag{3}$$

where V_{P0} = average V_P, V_{S0} = average V_S, and ρ_0 = average ρ.

Further, Whitcombe et al. (2002) extended linearized EI AVO crossplot projections by replacing $\sin^2 \theta$ with $\tan \chi$. In this new domain of EEI, the projections can be rotated from −90° to +90° through the rotation angle χ:

$$EEI(\chi) = V_{P0}\, \rho_0\, [(V_P/V_{P0})^p\, (V_S/V_{S0})^q\, (\rho_p/\rho_0)^r], \tag{4}$$

where $p = \cos \chi + \sin \chi$, $q = -8k \sin \chi$, and $r = \cos \chi - 4k \sin \chi$. The crossplot projections for EEI are generally presented as rotations of an axis relating gradient G (B in equation 1) plotted versus intercept R_0 (A in equation 1). To the extent that the two-term approximation is valid, any arbitrary elastic property can be estimated from the amplitude found at an appropriate rotation angle χ.

Whitcombe et al. (2002) demonstrated that important rock-physics parameters correspond to optimal χ angles. They used Gardner's rock parameters (Gardner et al., 1974) to calculate optimal χ angles for bulk modulus $\chi = +12.4^\circ$ and Lamé's parameter $\chi = +19.8^\circ$, but both can be within the range from $\chi = +10^\circ$ to $\chi = +30^\circ$. The shear modulus corresponded to $\chi = -51.3^\circ$ but could be within the range $\chi = -30^\circ$ to $\chi = -90^\circ$ depending on petrophysical properties of the formation. Those authors proposed using angles $\chi = +12.4^\circ$ and $\chi = -51.3^\circ$ to discriminate geologic parameters such as fluid and lithology, respectively (Table 1). This concept is commonly used in exploration and field development studies (see, for example, cases cited in Simm and Bacon, 2014).

Monitoring of producing hydrocarbon reservoirs using time-lapse seismic data has been of interest for field development. For example, Tura and Lumley (1999) applied a method to discriminate between reservoir pressure and water saturation changes using time-lapse seismic data for a field in the Gulf of Mexico, based

[1]Curtin University, Perth, Western Australia. E-mail: sergey.shevchenko@postgrad.curtin.edu.au; sergeys@sis-exploration.com.
[2]Michigan Technological University, Houghton, Michigan. E-mail: wayne@mtu.edu.

on P-wave AVO using prestack inversion that inverted for impedance changes of both P-waves and S-waves. They also demonstrated that using AVO time-lapse data can identify changes in the shear modulus, generally sensitive to pressure, and changes in the bulk modulus, sensitive to fluid saturation (but also to pressure). The method allowed quantitative estimates of pressure and saturation in the reservoir by calibrating the seismic amplitudes in the time-lapse AVO crossplots with well production under the assumption that only pressure and/or saturation significantly changed during production.

Previous studies have been undertaken at Enfield Field, where our approach is tested and where high-pressure water-injection assisted production. Two studies are of particular interest here. In the first, Smith et al. (2008) monitored pressure and saturation effects as the results of production using time-lapse seismic data. They identified differences as "soft" and "hard" amplitude changes from full-stack data as pressure and saturation changes, respectively. They also modeled pressure and saturation changes for appraisal wells, using log-based models, core data, and synthetic seismic data with the results as intercept and gradient plot for each well. Water saturation and pressure changes were identified at $\chi = +60^\circ$ and $\chi = -50^\circ$, respectively, from four wells. Then they used modeling results to create pseudo-pressure and pseudo-saturation differences as attribute maps.

Saul and Lumley (2015) also studied changes in pressure at Enfield using time-lapse seismic data. They developed a method based on rock-physics diagnostics to define the pressure sensitivity of rock properties, including changes in the grain-to-grain contact cement. They observed the changes in near- to mid-angle stacks' seismic amplitudes and velocity changes within the reservoir as the result of pressure increase and suggested that the weakening of the sandstone matrix is the basis for these changes. Some other efforts to apply EEI to time-lapse seismic data were presented by Dai and Mei (2014), who briefly presented an application for the estimation of fluid-saturation and fluid-pressure changes to an offshore Angola oil field, and Chakrabortya et al. (2020), who used modeled log data in a hypothetical case.

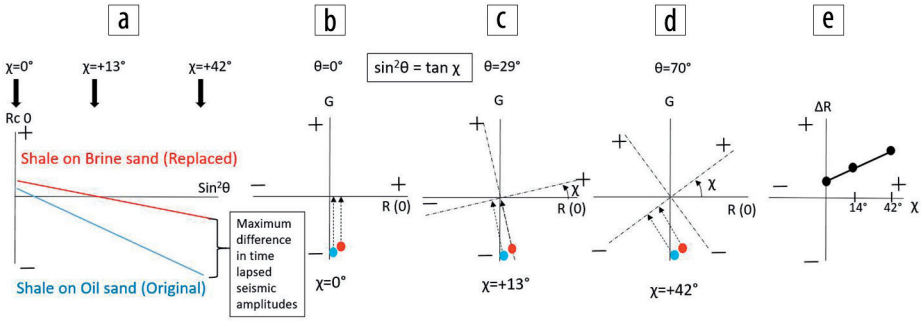

Figure 1. Simple model of shale over sand interface for time-lapse data due to a change in saturation only (oil to water as a result of brine injection). This and the following two figures also present the model at three χ angles for rotated intercept/gradient volume corresponding to three different projection domains as well as a summary diagram for three rotation angles of interest in each scenario. See text for detailed explanation.

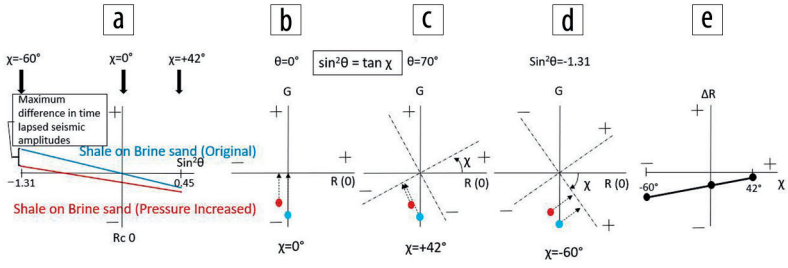

Figure 2. Simple model of shale over brine sand interface for time-lapse data due to a change in pressure only (as appropriate in the water sand below OWC) shown in presentations similar to those in Figure 1.

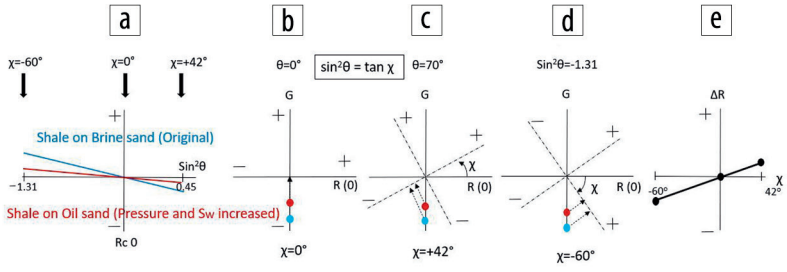

Figure 3. Simple model of shale over sand interface for time-lapse data due to changes in both pressure and saturation shown in presentations similar to those in Figure 1.

Proposed hypothesis and methodology

We propose a method to utilize time-lapse seismic data to differentiate fluid changes from pressure changes, and we implement it on publicly available data from Enfield Field. It is based on the use of EEI for prestack seismic data, using angle rotations designed to optimize observation of changes in these two parameters. We construct the angle rotations from ΔR_0 (intercept) and ΔG (gradient) domains as the difference of monitor survey minus base survey observing the amplitudes from seal-reservoir interface interpreted for both volumes. Figures 1–3 (inspired by the figures of Simm and Bacon, 2014) show three simple model scenarios of changes within the reservoir due to production: fluid-saturation change for oil sand to brine sand due to injection (Figure 1), fluid-pressure increase in brine sand below the oil-water contact (OWC) due to injection (Figure 2), and changes in both saturation and pressure in the oil sand due to injection (Figure 3). Within each of these figures, (a)–(e) demonstrate AVO crossplot projections as follows: (a) shows the linearized two-term AVO plotted against $\sin^2\theta$; (b) shows where the slopes of those lines and their intercepts would appear on an intercept-gradient plot, and the dashed lines show the zero-offset amplitudes, labeled as $\chi = 0^\circ$; (c) and (d) show the same points as in (b) but with dashed lines indicating the amplitudes falling

on an axis rotated by χ, with angles chosen for each scenario; and (e) shows the amplitude differences (red points minus blue points), as rotated to $\chi = 0^\circ$, $+42^\circ$, and $+13^\circ$ or -60° as appropriate for the scenario. All data and illustrations in this paper use positive standard polarity (Sheriff and Geldart, 1995), in which a positive zero-offset reflection coefficient corresponds to an increase in AI.

Pressure changes. We recognize that the shear modulus is unaffected by fluid changes in the formation, as assumed in Biot-Gassmann modeling, but the shear modulus is affected by changes in effective confining pressure. As a result, a time-lapse change observed in EEI at an angle corresponding to shear modulus should indicate changes in effective confining pressure and not changes in fluid content. This implies that the χ angle for the shear modulus should be 90° from the angle for fluid changes; this observation may be useful in evaluating other predictions of optimal angles or the validity of Biot-Gassmann and other assumptions in any individual study. The angle χ corresponding to the shear modulus can be calculated from log data and is often found to be -50° to -60° (Whitcombe et al., 2002), and can be estimated from log data for any reservoir under consideration.

On the other hand, a separate approach can be made to find the angle most sensitive to pressure changes that can incorporate the combined effects on shear and bulk moduli, even though that angle may not be 90° from the fluid-saturation angle. This can be accomplished through laboratory studies of core samples, or by making assumptions of the lithology and using comparisons with other rocks, similar to those in the reservoir under consideration, whose pressure response is known. The investigator will need to use his or her judgment to decide which approach for pressure-change prediction (shear-modulus angle or most-sensitive angle) to use in any given study. It may depend on what data are considered more reliable, and it may be advisable to use both approaches and compare the results.

Fluid-saturation changes. Through Biot-Gassmann, we know that the bulk modulus is affected by fluid changes. We know that the bulk modulus is also affected by changes in fluid pressure, so the bulk modulus alone should not be used as the fluid indicator in time-lapse studies where appreciable pressure changes may be expected. Perhaps the most straightforward method is to model the predicted changes in elastic properties (and AVO behavior) from fluid substitutions based on log data and use the rotation angle that is found to be optimal to observe those changes. Alternatively, one could use the angle that is orthogonal to that which is most sensitive to changes in pressure; this angle would be sensitive to anything but pressure, and because we assume only fluid changes and pressure changes take place in the reservoir, that angle would correspond only to fluid changes, even if it is not optimally sensitive to them.

A note on orthogonality and optimal sensitivity: in a world designed for the convenience of geophysical interpreters, the χ angles most sensitive to pressure changes and to fluid changes would be 90° apart. Unfortunately, it appears that in many cases the angles are nearly orthogonal, but not quite. The investigator may wish to examine five angles, two of which are optimally sensitive to pressure changes and to saturation changes, two of which are orthogonal to those, and the angle for shear modulus. One would hope that the angle optimal for saturation changes is nearly orthogonal to that for shear modulus, in which case those are the only two angles needed. One's definition of "nearly orthogonal," however, should be backed up by comparisons with results from the other angles for any given reservoir.

Application to a case study

Background. The Enfield oil field, which is no longer under production, is located in the offshore Carnarvon Basin in Western Australia. The field is a northeasterly dipping structure sealed laterally by two major normal faults (Figure 4). The reservoir rocks are Late Jurassic "soft" Macedon Sandstone of average 24% porosity sealed by "hard" Macedon Mudstone. The reservoir consists of an upper reservoir of amalgamated turbidites with 10–25 m thickness and a lower reservoir of locally developed channelized turbidites with thicknesses greater than 50 m. The two are separated by 1–2 m thick shales interpreted as a major flooding surface. Numerous faults combined with the thin reservoir and a complex depositional architecture create limited fluid flow pathways, baffles, and barriers that are difficult to predict (see Hamson, 2012, for log-based cross sections and Smith et al., 2008, for general observations).

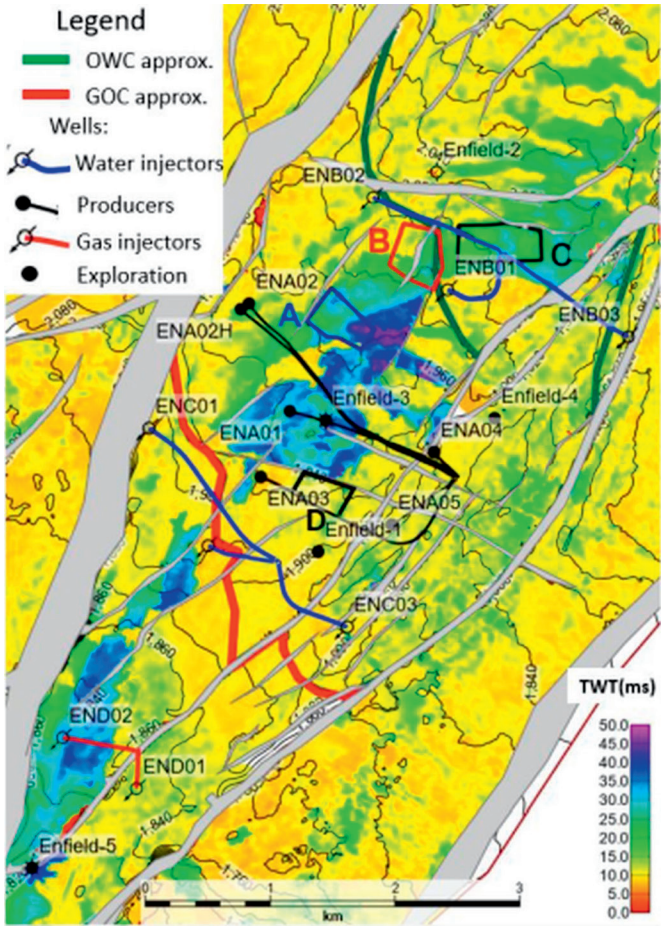

Figure 4. Enfield two-way-time structural map shown as labeled contours to Top Macedon Sandstone (ms) with color representing isopach thickness of the Macedon sand reservoir. The polygons labeled A, B, C, and D are areas in which quantitative studies were conducted, and injection and production wells at the time of monitor survey are shown. General dip is down to the northeast. Thin-bed artifacts in the seismic data are likely to be present where isopach thicknesses are less than 10 ms.

DOI:10.1190/tle41110777.1

Enfield was chosen because it was developed using high-pressure water injection, some of which was injected below the original OWC where the formation experienced strong fluid-pressure changes without a change in fluid content. Other areas, within the oil reservoir itself, underwent both pressure and fluid changes. In addition, earlier time-lapse seismic studies have shown that the formation is pressure sensitive (Smith et al., 2008; Bentley, 2010; Saul and Lumley, 2015).

The base seismic survey was conducted in 2004, prior to development of the field. In 2007, at the time of the monitor acquisition used here, the field had three horizontal and two deviated oil producers, two gas injectors in the gas cap, three deviated water injectors at the OWC, and three deviated water injectors at the gas-oil contact (Figure 4). All of the geologic and field development technical complexities mentioned earlier make attempts to use time-lapse seismic data for predicting saturation and pressure changes particularly valuable as well as challenging.

Data quality and availability. The processed data sets that previous investigators used were not available to us, but we located two publicly available sets of data suitable for our use. These data sets were based on the same base and monitor field recordings as some of the other studies, but because the technology for time-lapse processing was still being developed at the time these data sets were processed, they are of poorer quality than the reprocessed data used by other studies. We use an initial base seismic survey "BaseP" that was acquired in 2004 and a monitor "M1P" survey that was acquired in 2007, seven months after the field commenced oil production. (We use the "P" designation to emphasize that these processed data sets are not the same as the reprocessed data used by other investigators.) The operator also conducted two additional time-lapse monitor surveys, in 2008 and 2011, which we could not access but which are referenced in other studies. The two surveys that we used, BaseP and M1P, were processed with AVO studies in mind, using identical workflows, intended for monitoring changes in the reservoir due to production (Wickham et al., 2008). The data consisted of partial stacks at near (8°–18°), mid (19°–30°), far (30°–41°), and ultra-far (41°–51°) angle ranges and are of only fair quality for AVO application (Chan et al., 2009). We improved the data by applying residual moveout processing, resulting again in near, mid, far, and ultra-far stacks. We did not use the ultra-far stacks in our studies due to their low quality.

The reliability of seismic volumes to be used for time-lapse studies can be gauged by measuring the repeatability as a normalized root mean square (NRMS) (Kragh and Christie, 2002). Because we found that the repeatability varied with angle range, we also calculated NRMS for intercept and gradient volumes and for the seismic volumes after rotation to χ angles of interest to us. We found that the intercept volume demonstrated high repeatability (low NRMS values), but the gradient volume was less repeatable. As a result, the volumes rotated to small angles also showed high repeatability, but the volumes rotated to larger angles showed lower repeatability; the large-angle rotations should be used cautiously (Figure 5).

Seismic data processing and interpretation. Enfield-1, -2, -3, -4, and -5 exploration and appraisal wells (Figure 4) were used for structural interpretation, and Enfield-2, -3, and -4 wells, with publicly available full arrays of logs, were used in AVO and inversion processing and interpretation. Top Macedon Sand horizon exhibits time shifts between the BaseP and M1P surveys up to –10 ms, mainly around injectors. This appears to be the result of the collapse of the top reservoir due to high injection pressure damaging the formation by weakening grain contacts (Saul and Lumley, 2015). Therefore, rather than subtract one three-dimensional volume from another, we used values extracted along horizons within the BaseP and M1P volumes separately and then obtained their differences (always subtracting the values of BaseP from M1P). Model-based EEI inversion was calculated using preproduction logs for both the BaseP and M1P surveys. Commercial software was used for the seismic data processing and for the inversion and modeling.

Previous investigators (Bentley, 2010; Saul and Lumley, 2015) found that thin-bed effects tended to overwhelm the AVO response in many parts of the field. Our observations are consistent with that, so we restricted our detailed analyses to areas where the beds are thick. We have chosen three polygons within thick-bedded portions of the field where we test our model quantitatively. Polygon A is in the vicinity of the producer wells, equally away from the southern and northern injectors (Figure 4); here we anticipated only small changes in either the pressure or saturation. Polygon B is within the oil leg just above the OWC where we expect an increase in both water saturation and pressure due to the nearby injector ENB01. Polygon C is within the water leg and close to injector ENB01 where we anticipate a large increase in pressure but no change in saturation.

To determine the optimal EEI angle χ for our fluid-saturation discriminant, we took advantage of fluid-substitution calculations conducted by the operator for the pay zone in the Enfield-2, -3, and -4 wells. The operator had used Gassmann fluid substitution, log data, and perhaps other insights available to them to make these substitutions (Martin, 2002). We then used the AI versus gradient impedance (GI) crossplot method proposed by Whitcombe and Fletcher (2001), calculating ln(AI) versus ln(GI) at each depth point, where AI is EEI at 0° and GI is EEI at 90°, obtaining χ = +42° as that angle which connects (on average) the points before and after fluid substitution. This is used as the mean optimal rotation angle to identify fluid changes. Because we are concerned with the effects of water flooding, we used the change from oil to brine and gas to brine for each depth data point and averaged them (Figure 6).

While +42° is predicted to be optimal for fluid changes, the angle orthogonal to it, –48°, should be that angle

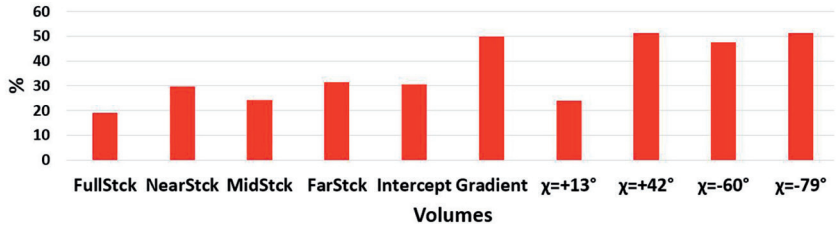

Figure 5. NRMS for seismic volumes in polygon A for a time window covering the 700 ms immediately above Top Macedon.

DOI:10.1190/tle41110777.1

that is completely unaffected by fluid changes and, therefore, affected only by pressure changes, subject to the caveats mentioned earlier. That angle may or may not be the one that is most sensitive to pressure changes, however.

To determine the EEI angle most sensitive to pressure changes, we used the Enfield rock-physics model by Wulff et al. (2008). This model is based on fitting laboratory velocity-pressure data measured on well core plugs to MacBeth's (2004) model for dry and brine-saturated sandstones, fitting a curve to the data points. The publicly available data were limited to normalized velocities and pressures. We simply assumed that they could be applied to in-situ Enfield-2 well pressure and log data, and solved for useful velocity-pressure pairs (Figure 7a). Then we used these data to calculate ln(AI) and ln(GI) to determine the angle of maximum sensitivity, $\chi = -79°$, to changes in pressure (Figure 7b), again simply connecting the points at different pressures. The ΔEEI values at each point (used in the next section of this paper) were calculated using the equation for EEI (equation 4) and plotted, along with values for ΔP (in psi) on the crossplot (Figure 7c), and plotted again as ΔP versus ΔEEI in Figure 8.

For completeness and for comparison with other studies, the χ angles for $\Delta\mu$ ("mu," shear modulus), ΔK (bulk modulus) and $\Delta\lambda$ (Lamé parameter "lambda") were calculated using commercial software and as suggested by Whitcombe et al. (2002) using Gardner's relationship. These angles, as well as the results of our modeling for optimal fluid angle and optimal pressure angle, are summarized in Table 1. We note that the angle (–48°) orthogonal to that which we had obtained for fluid sensitivity is close to those predicted for changes in the shear modulus (–51.3° or –60°), as one would hope to find.

Pressure and saturation calibration to EEI units. Seismic volumes rotated to various EEI angles can be interpreted qualitatively or quantitatively. To provide a qualitative interpretation, one can use difference volumes based either on inverted results (which provide actual units of impedance, albeit of an "elastic" version) or on simple rotations from R_0 (or A, the zero-offset reflection amplitude) and G (or B, the AVO "gradient"). While the latter approach, referred to here as the "reflectivity" method, is straightforward, and its results discussed in the following section, the approach using inverted volumes requires additional explanation.

A quantitative interpretation requires a relationship between the values obtained at the rotated angles and the parameters of

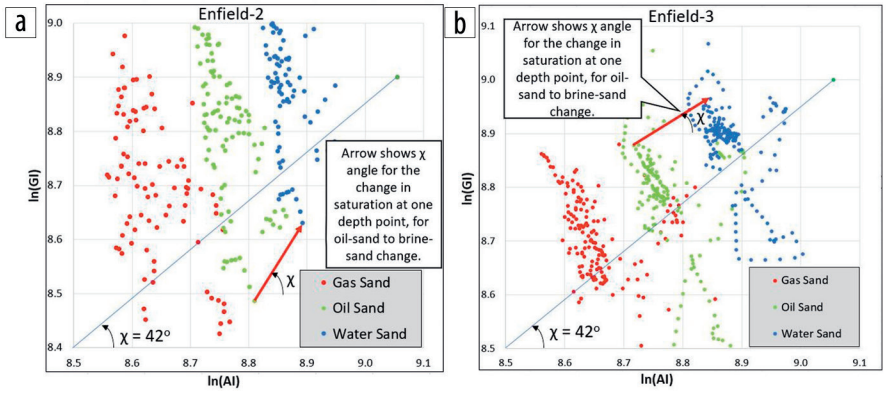

Figure 6. The ln(AI) versus ln(GI) crossplot calculated from Enfield-2 and Enfield-3 fluid-substitution results and the average angle $\chi = +42°$ is shown as a vector from the origin. A single example of the change experienced by one specific data point is shown for each well for oil sand to water sand; the average of all such changes yields the +42° angle.

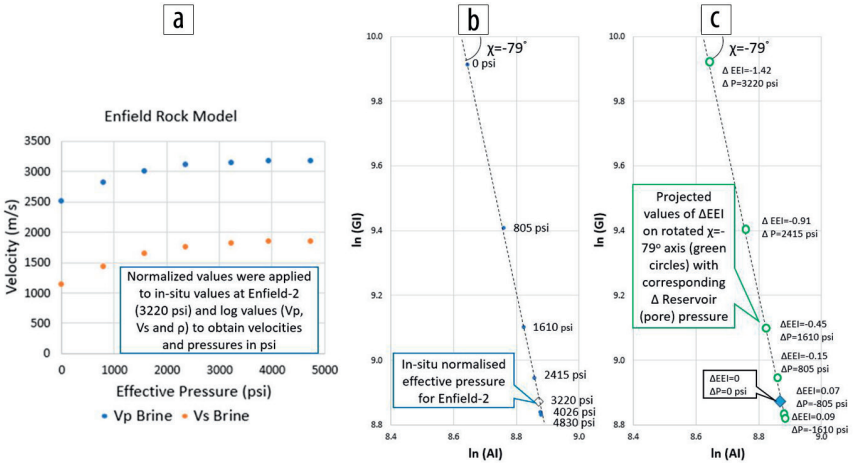

Figure 7. Pressure-velocity calibration. (a) The model was fitted to (psi) pressure units using Enfield-2 in-situ pressure condition (3220 psi). (b) Calculation of optimal χ angle for pressure changes using the velocities in (a) and appropriate densities to find ln(AI) and ln(GI), and, in turn, the best-fit line through those points. (c) ΔEEI and ΔP (pressure) values projected on the $\chi = -79°$ axis.

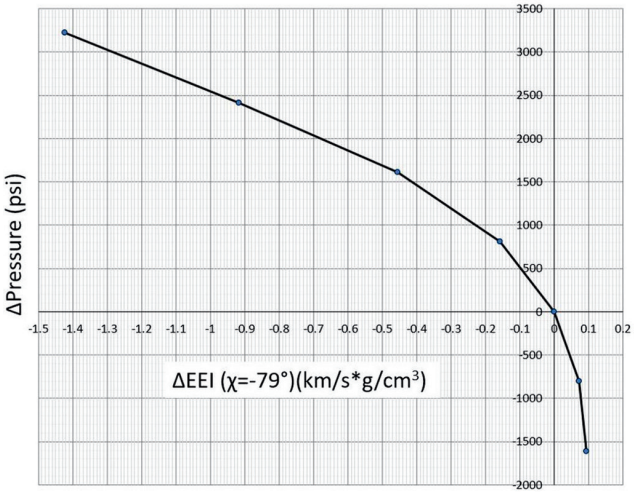

Figure 8. ΔP (psi) related to ΔEEI ($\chi = -79°$) enabling a relationship from EEI units to pressure units for the reservoir (pore) pressure change between BaseP and M1P surveys. A piece-wise approximation to the curve was used for computation of the values between the points.

interest, such as the fractional change in water saturation or the change in pressure in psi. These can be predicted from EEI calculations using the fundamental EEI equation (equation 4). However, it is important to remember that the application of these relationships across the reservoir will depend on the original calibration of optimal rotation angles. The caveats and factors such as clay content and thin-bed artifacts in the reservoir that may affect the results are not discussed in detail in this paper.

To relate our seismic difference observations to changes in saturation, we made some simple assumptions, applicable to either the reflectivity or inverted volumes. Because of these assumptions, required due to our limited knowledge of the formation properties, we refer to a fractional change in saturation, over the range of movable-oil saturation, as the "movable-oil saturation" change, or ΔSw_M. First, we assumed that the area immediately surrounding injection well ENB02 was fully swept and underwent change from irreducible water saturation (probably about Sw = 20%) to residual oil saturation (probably about Sw = 80%). We assigned the value observed at this location for the change in reflectivity and the change in EEI to be $\Delta Sw_M = 1$ or 100% (of movable oil, fully swept) and note that a difference value of $\Delta Sw_M = 0$ corresponds to no fluid change (unswept). Because the Biot-Gassmann curves are roughly linear for the substitution of water for oil (as both are liquids) over this saturation change, we assumed a linear relationship between seismic reflectivity or EEI changes and saturation (Figure 9); note that the entire range of ΔSw_M values from 0 to 1 likely covers only a fractional change in Sw from 0.2 to 0.8. We must also remember that because the EEI angle of +42° is not exactly orthogonal to the angle of maximum sensitivity to pressure changes (–79°), there is some nonzero effect due to pressure changes.

Table 1. EEI optimal χ angles for rock-physics parameters estimated using various approaches.

Method of calculating EEI χ angle	Optimal χ angle (degree) for parameters:				
	K	Mu	Lambda	Fluid	Pressure
Commercial software for Enfield wells	+13	–60	+21		
Whitecombe et al. (2002) for Gardner's parameters	+12	–51.3	+19.8		
Smith et al. (2008), using Enfield wells data				+60	–50
Gassmann fluid substitution using logs				+42	
Rock-physics model from core samples lab data					–79

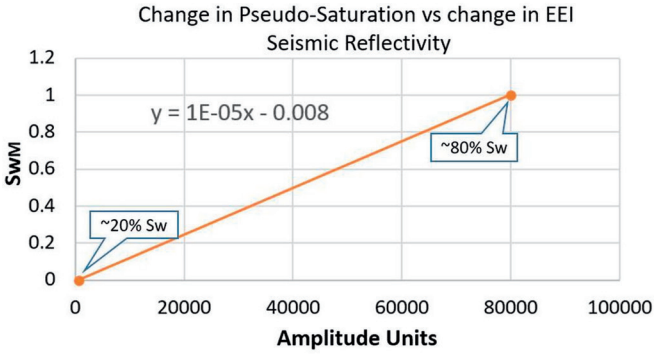

Figure 9. Graph used to calculate the changes in ΔSw_M (movable-oil-saturation change) from ΔEEI units, calibrated at the two end points as described in the text.

Results and discussion

We concentrate on differences resulting from (M1P – BaseP) in the three polygons: A (where only small changes in fluid pressure or saturation are expected); B (where significant changes in both saturation and pressure are expected); and C (where 100% water saturation is expected to remain constant while the fluid pressure increases significantly). We specifically examine rotation angles predicted to be appropriate, in this reservoir, for changes in fluid saturation (χ = +42°) and for changes in fluid pressure (χ = –79°).

First, we qualitatively examine averages based on our results in a (ΔR_0, ΔG) crossplot (Figure 10). Three data points, each representing average values in one polygon, are identified by colors (A: blue; B: red; C: black); those colors are also used for the associated thin solid lines projected to the rotated axes. We also have two thick dashed lines representing the rotated axes (fluid-saturation change at χ = +42° is pink, and fluid-pressure change χ = –79° is green). (Note that in our convention, net-pressure changes in the upper left quadrant correspond to negative values on that axis, having been rotated in the "negative" direction; these in turn correspond to increases in fluid pressure.)

We start with the simplest case. Polygon C (black dot) represents an area located in the water leg where no changes in water saturation

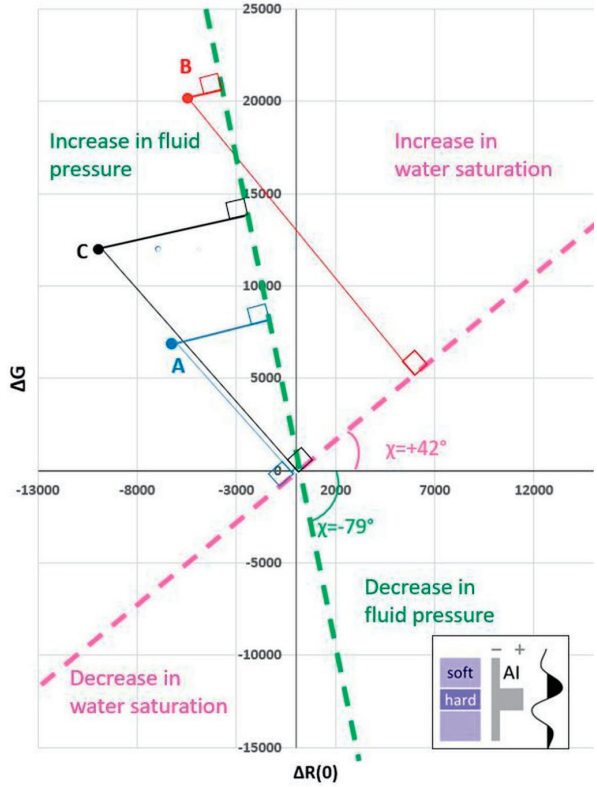

Figure 10. Time-lapse seismic amplitudes differences (M1P – BaseP) for average values in polygons A (blue), B (red), and C (black) shown as a (ΔR_0, ΔG) crossplot. Rotated projections for fluid-saturation changes at χ = +42° and for fluid-pressure changes at χ = –79° are displayed as thick pink and green dashed lines, respectively. Thin solid lines show the paths of projection from each polygon's point to each rotated axis.

are expected. We see that the projection onto the χ = +42° axis (pink; fluid changes) demonstrates a vanishingly small amplitude, corresponding to essentially no change in saturation. We also see that the projection onto the χ = −79° axis (green; pressure changes) is quite large, suggesting a large increase in fluid pressure.

Polygon A (blue dot) represents an area in the oil leg distant from any injecting or producing wells, and we might expect only small changes, if any, in fluid saturation and modest increases in fluid pressure. This also shows a vanishingly small amplitude on the χ = +42° axis, corresponding to essentially no change in saturation, but a moderate amplitude on the χ = −79°, suggesting a modest change in fluid pressure as the polygon, which is reasonable as the polygon is far away from the injectors.

Polygon B is located in the oil leg, close to the OWC and the water injector ENB01, where we expect to observe a significant increase in water saturation during initial production and a very large increase in fluid pressure. The projections onto both rotated axes suggest that the largest increases in both water saturation and fluid pressure among the three polygons are indeed observed in this area.

Polygon-wide averages were also computed for the ΔEEI inversion results. These were computed from inversions that were conducted on the BaseP and M1P volumes separately, and then differenced over the interval Top-Bottom Macedon. The resulting difference values were averaged over each respective polygon. The results are less consistent with expectations than the (ΔR_0, ΔG) crossplot shown in Figure 10, probably due to the many assumptions required for inversion of data of limited bandwidth; for example, polygon C, below the OWC, shows a response suggestive of decreased water saturation on the inversion results, which is unlikely.

The polygon-wide average results for both the time-lapse reflectivity differences (ΔR_0, ΔG) and the inverted ΔEEI are summarized in bar graphs (Figure 11) for the optimal χ angles for fluid changes and pressure changes as well as χ angles for $\Delta\mu$, ΔK, and $\Delta\lambda$, for comparison with other rotations commonly used for exploration purposes.

Several points can be highlighted from the qualitative results:

- The relative values from seismic reflectivity for each polygon are consistent with expectations, given a qualitative interpretation of reservoir production.
- The inversion results are mostly consistent with expectations, except for polygon C at χ = +42° (saturation change), which suggests an unreasonable time-lapse response. The many assumptions required for inversion of older, narrow-band seismic data are likely responsible.
- The shear modulus ($\Delta\mu$, at χ = −60°) provides results similar to that for pressure (χ = −79°), as one might anticipate, particularly for reflectivity.
- The rotation angles often found to be useful for exploration and development (ΔK, at χ = +13°; $\Delta\lambda$, at χ = +21°) appear to be much less useful for time-lapse monitoring of fluid-saturation and fluid-pressure changes.

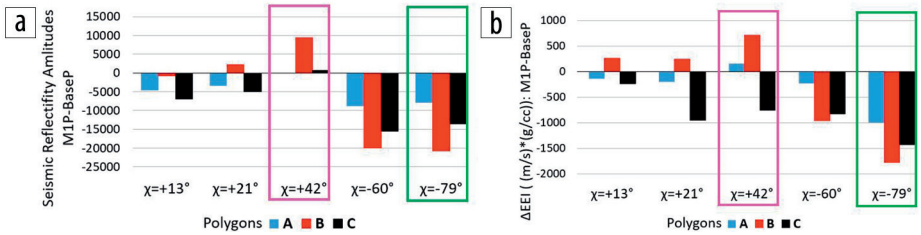

Figure 11. (a) Time-lapse seismic reflectivity and (b) inversion amplitude differences as average values versus χ angles for polygons A, B, and C. Optimal angles χ = +13°, χ = +21°, and χ = −60° relate to ΔK, $\Delta\lambda$, and $\Delta\mu$, respectively. The most sensitive angles for saturation and pressure changes are χ = +42° and χ = −79°, respectively, emphasized by the pink and green boxes.

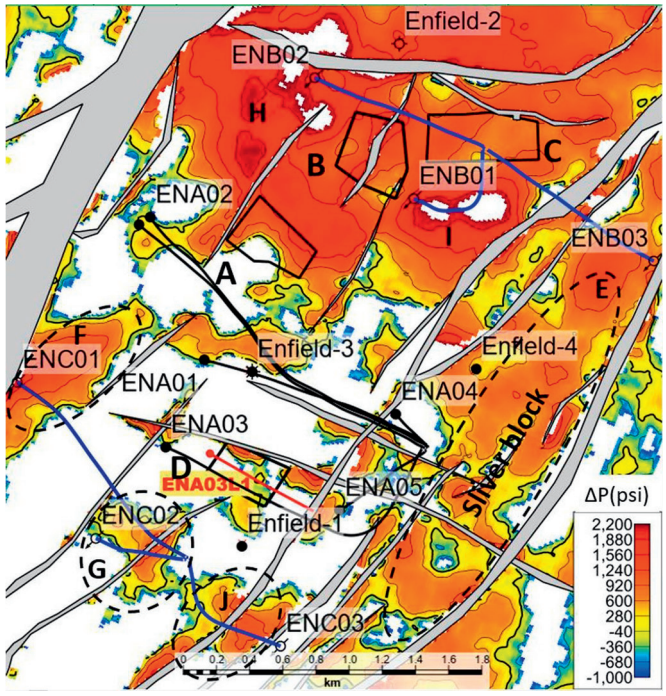

Figure 12. Reservoir fluid-pressure change ΔP (psi). Contour interval ΔP = 500 psi. Thick contour is 0. White color represents null values. (Polygon D was added for comparison with pressure obtained during drilling of well ENA03L1).

Additionally, another method of determining optimal rotation angles was tested, based on "scanning" for the largest effect in an area where only certain pressure or fluid changes may be expected. The method was not presented here in the interest of brevity.

Limited quantitative data were available for pressures within the field, and none for water saturation. First, we calculate the predicted change in pressure at polygon C where we do not expect any change in water saturation (below OWC). Application of the fundamental EEI equation to the average change in EEI found at polygon C predicts a fluid-pressure increase of about 1500 psi. Estimates of pressure change in that polygon from the operator or other researchers (with additional information not available to us) are varied, at +970 psi, +1450 psi, +1500 psi, and +1700 psi. It seems that our prediction may be fairly accurate, or, at most, require a modest calibration. A comparison of our predictions

Table 2. Pressure estimate for polygon C of +970 psi was used to scale the ΔEEI inversion results for pressure calculation. Polygons B and D are examined here for quality control. "P (discovery)" is the original pressure value at time of discovery from five wells calculated at the depths of the reservoir at the locations of polygons B, C, and D. "P (monitor)" is the pressure at the time of the monitor survey for B and C displayed by the operator on a map (Smith, 2008) pressure value for D was obtained from a nearby well, drilled a few months after the monitor survey.

Polygon	Polygon status	Depth (m)	P discovery (psi)	P monitor (psi)	ΔP from operator (psi)	ΔP from ΔEEI (psi)	Discrepancy (psi)	Error %
B	"Blind" test	2130	3142	<4200	>+1058	+1224	+166	<16
C	Used for scaling	2190	3230	4200	+970	+958	–12	1
D	"Blind" test	2060	3020	3200	+180	+63	–117	65

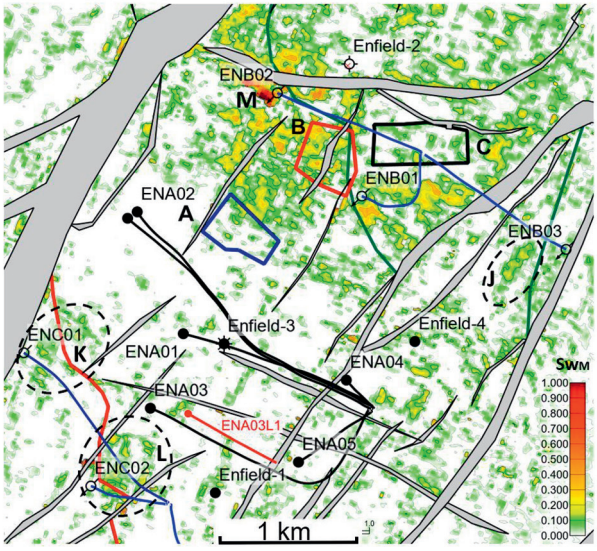

Figure 13. Movable-oil-saturation change ΔSw_M. Solid highlighted contour $\Delta Sw_M = 0.1$.

with a map published by the operator (Smith, 2008), using a relationship calibrated to +970 psi on that map for polygon C, are summarized in Table 2 for three polygons. Note that polygon D, which was added for this test in order to compare our prediction with fluid pressures measured in a well drilled a few months after the monitor survey, may be affected by thin-bed effects, which resulted in "null" values seen in Figure 12.

The "ΔP from ΔEEI (psi)" in the table was calculated for each bin within polygons and then averaged (averaging differences account for the 1% "error" in polygon C). The small discrepancy of less than 16% for polygon B is a good result for pressure prediction. The discrepancy of 65% error for polygon D is large but still satisfactory given the small values involved and the possible thin-bed effects. The map shows that all water injectors including ENC01, ENC02, ENB02, ENB01, and ENB03 have anomalous pressure around the wells labeled F, G, H, I, J, and E, respectively (Figure 12). It is worth drawing attention to pressure anomaly E over the Sliver block on Figure 12. The operator recognized (Smith, 2008) the pressure increase at this block and drilled a producer well updip of ENB03 in 2008 to recover unswept oil from this block (Hamson, 2012).

The movable-oil-saturation change ΔSw_M map generated from our reflectivity volumes also correlates well with the expected increase in saturation around water injection wells at K (well ENC01), L (well ENC02), M (well ENB02), and J (well ENB03) above the OWC (Figure 13); a numeric comparison is not possible due to the lack of ground-truth data. Anomaly L is worth emphasising, as it likely caused water encroachment resulting in the shutting down of producer ENA03 and injector ENC02, consistent with the operator's interpretation (Smith et al., 2008). Thin beds (see Figure 4) in the vicinity of the ENB01 injector below the OWC present artifacts that appear as an (unreasonable) increase in saturation within the water leg.

Conclusions and recommendations for use of this technique

We have demonstrated that the EEI method applied to time-lapse seismic data can be used to monitor reservoir pressure and saturation changes during production. In a case study, the method successfully predicted the areas where changes in pressure and/or saturation were expected and did a good job of separating the two properties. Our final calculated pressure maps were tested successfully with two areas of changing pressure that had not been used in the calibration, showing that our quantitative results are credible. Additionally, our anomalies of pressure and saturation change coincide with the results from the operator and other researchers who used different methods to map pressure and saturation changes for the field.

The ease with which rotated seismic volumes, to any arbitrary χ angle, can be created in modern workstation software, could make the reflectivity (ΔR_0, ΔG) method a useful and quick technique to include in the time-lapse interpreter's toolbox for use in any reservoir. The use of modern high-quality data should provide results better than those we obtained here.

A proper analysis of NRMS for various acquisition angle ranges and for rotation χ angles should inform the interpreter which results should be treated with caution.

We suggest several methods to find optimal χ angles for reservoir pressure and saturation changes. In the absence of good rock-physics studies, one could use the optimal angle for shear modulus to detect pressure changes and an orthogonal angle to this to detect saturation changes. Neither angle would be that which is most sensitive to each property, but they are uniquely uncontaminated by the other property. When one has the opportunity to conduct more detailed analysis, the optimal angles for each property could be determined and studied; the closer they are to orthogonal, the better.

Our techniques may prove helpful for quick-turnaround studies and for obtaining confidence in any more detailed analyses. The results we obtained in the case study were based on mediocre-quality data that happened to be available online years after the field surveys were conducted. They did not include higher-quality processing or later surveys that had been made available in the past but that are no longer accessible to researchers. We look forward to seeing similar studies performed on modern high-quality data by other researchers interested in testing these concepts. TLE

DOI:10.1190/tle41110777.1

Acknowledgments

DownUnder GeoSolutions and GeoSoftware/HampsonRussell are gratefully acknowledged for providing interpretation software for this project. M. Sams brought some relevant papers to our attention, which we appreciate. W. D. P. was supported by a Fulbright scholarship during part of this work, and he expresses gratitude to the Australian-American Fulbright Commission and to the administration of Curtin University. The authors thank Boris Gurevich for suggesting the use of Enfield Field and for discussions that improved the study.

Data and materials availability

Data and associated reports are available through the Geoscience Australia repository; last accessed on 10 December 2021 through http://www.ga.gov.au/nopims with searches for "Enfield" surveys and wells. Additional supporting aspects of this research, some briefly referenced in the paper, are available from the corresponding author.

Corresponding author: sergeys@sis-exploration.com

References

Bentley, R., 2010, Simultaneous analysis of the seismic time shifts and amplitude changes due to water injection: Curtin University of Technology, Department of Exploration Geophysics, Report GPH 4/10.

Chakraborty, S., R. Chatterjee, and A. Yadav, 2020, Time lapse rock physics template and seismic quantitative analysis amid the production phase: Journal of Applied Geophysics, **174**, 103956, https://doi.org/10.1016/j.jappgeo.2020.103956.

Chan, C., J. Sun, S. Birdus, K. M. Lee, O. Tang, and M. Wang, 2009, Enfield 4D survey, Northwest Cape, Western Australia, seismic data processing report: CGGVeritas, Veritas Geophysical (Asia Pacific) Pty. Ltd.

Connolly, P., 1999, Elastic impedance: The Leading Edge, **18**, no. 4, 438–452, https://doi.org/10.1190/1.1438307.

Dai, X., and L. Mei, 2014, Time-lapse extended elastic impedance application in estimation of fluid saturation and pressure changes: International Geophysical Conference & Exposition, SEG and CPS, Global Meeting Abstracts, 974–977, https://doi.org/10.1190/IGCBeijing2014-246.

Gardner, G. H. F., L. W. Gardner, and A. R. Gregory, 1974, Formation velocity and density — The diagnostic basics for stratigraphic traps: Geophysics, **39**, no. 6, 770–780, https://doi.org/10.1190/1.1440465.

Hamson, G., 2012, Leveraging 4D seismic and production data to advance the geological model of the Enfield oil field, Western Australia: Search and Discovery Article 20172, adapted from oral presentation at Annual Convention and Exhibition, AAPG.

Hendrickson, J., 1999, Stacked: Geophysical Prospecting, **47**, no. 5, 663–706, https://doi.org/10.1046/j.1365-2478.1999.00150.x.

Kragh, E., and P. Christie, 2002, Seismic repeatability, normalized rms, and predictability: The Leading Edge, **21**, no. 7, 640–647, https://doi.org/10.1190/1.1497316.

MacBeth, C., 2004, A classification for the pressure-sensitivity properties of a sandstone rock frame: Geophysics, **69**, no. 2, 497–510, https://doi.org/10.1190/1.1707070.

Martin, P., 2002, WA271P well log summaries, Enfield-4, NOPIMS database, ID D00018561.

Saul, M., and D. Lumley, 2015, The combined effects of pressure and cementation on 4D seismic data: Geophysics, **80**, no. 2, WA135–WA148, https://doi.org/10.1190/geo2014-0226.1.

Sheriff, R. E., and L. P. Geldart, 1995, Exploration seismology (2nd edition): Cambridge University Press, https://doi.org/10.1017/CBO9781139168359.

Shuey, R. T., 1985, A simplification of the Zoeppritz equations: Geophysics, **50**, no. 4, 609–614, https://doi.org/10.1190/1.1441936.

Simm, R., and M. Bacon, 2014, Seismic amplitude: An interpreter's handbook: Cambridge University Press, https://doi.org/10.1017/CBO9780511984501.

Smith, M., 2008, Enfield 4D Monitor 1 2007 interpretation report, Woodside Company report.

Smith, M., A. Gerhardt, B. Mee, T. Ridsdill-Smith, A. Wulff, and L. Bourdon, 2008, The benefits of early 4D seismic monitoring to understand production related effects at Enfield, North West Shelf, Australia: 78th Annual International Meeting, SEG, Expanded Abstracts, 3159–3163, https://doi.org/10.1190/1.3064002.

Tura, A., and D. E. Lumley, 1999, Estimating pressure and saturation changes from time-lapse AVO data: 69th Annual International Meeting, SEG, Expanded Abstracts, 1655–1658, https://doi.org/10.1190/1.1820849.

Whitcombe, D. N., 2002, Elastic impedance normalization: Geophysics, **67**, no. 1, 60–62, https://doi.org/10.1190/1.1451331.

Whitcombe, D. N., P. A. Connolly, R. L. Reagan, and T. C. Redshaw, 2002, Extended elastic impedance for fluid and lithology prediction: 70th Annual International Meeting, SEG, Expanded Abstracts, 138-141, https://doi.org/10.1190/1.1815660.

Whitcombe, D. N., and J. G. Fletcher, 2001, The AIGI crossplot as an aid to AVO analysis and calibration: 71st Annual International Meeting, SEG, Expanded Abstracts, 219–222, https://doi.org/10.1190/1.1816574.

Wickham, J., B. Burmaz, L. Abzalov, and S. Malajczuk, 2008, Data processing report 4D seismic survey, Enfield 4D Northwest Cape, Western Australia for Woodside Energy Limited: PGS Data Processing A/P Pty. Ltd.

Wulff, A., A. Gerhardt, T. Ridsdill-Smith, and M. Smith, 2008, The role of rock physics for the Enfield 4D seismic monitoring project: Exploration Geophysics, **39**, no. 2, 108–114, https://doi.org/10.1071/eg08015.